

Full paper

Self-powered digital-analog hybrid electronic skin for noncontact displacement sensing



Hang Guo^{a,1}, Hanxiang Wu^{b,1}, Yu Song^b, Liming Miao^b, Xuexian Chen^a, Haotian Chen^a, Zongming Su^b, Mengdi Han^b, Haixia Zhang^{a,b,*}

^a Academy for Advanced Interdisciplinary Studies, Peking University, Beijing 100871, China

^b National Key Laboratory of Science and Technology on Micro/Nano Fabrication, Peking University, Beijing 100871, China

ARTICLE INFO

Keywords:

Electronic Skin
Noncontact
Self-Powered
Motion sensing
Electrostatic inductions

ABSTRACT

The fast progressing electronic skins are spreading their applications into many aspects of human life. In terms of motion sensing, drawbacks exist in state-of-the-art approach of integrating sensing units into arrays *e.g.* the tradeoff between resolution and effective area, power consumption and interacting experience. This paper presents a novel self-powered digital-analog hybrid electronic skin for measuring noncontact linear planar displacement which achieves a high resolution of (0.75 mm, 1.07 mm, 2.20°) in a large area of 100 cm² in three degrees of freedom. Owing to utilization of masked silver nanowires (AgNWs) spray coating and corona charging techniques in the fabrication process, this electronic skin is transparent and stretchable, while realizing self-powered sensing of an electret based on electrostatic inductions. Theory and localizing functions are proposed and proved by accordance with simulation and standard testing results. This electronic skin is capable of acting as an effective human-machine interface, which shows its future potential of practical usage in portable electronics, healthcare devices, and artificial intelligence, *etc.*

1. Introduction

The research on electronic skins is developing rapidly. Researchers apply intensive efforts to the construction of a solid and systematic study of multifunctional electronic skins [1–3]. This kind of skin mimicking device can measure major human-related signals *e.g.* perspiration [4], electroencephalograms [5], smell [6], humidity [7], temperature [8–10], and light [11]. In terms of mechanical sensing, pressure [12–15] and strain [16–19] are the two basic elements achieved in multiple mechanisms, on which more complicated hybrid sensing systems are built to measure vibration [20], torsion [21], motion of human [22], contact trajectory [23], pulse [24], *etc.* Electronic skins relying on contact sensing can measure a variety of environmental parameters, but they lack the flexibility in interacting modes due to the requirement of contact. As a result, contact sensing is not fascinating enough in terms of novel human-machine interfaces. The need for user-interacting experiences and convenience calls for electronic skins featuring noncontact sensing methods. Based on electrostatic inductions, noncontact sensing mechanisms improve the degree of freedom for interaction purpose [25]. While analog sensing methods [26] elevate the resolution, and digital arrays increase sensing area. Current state-of-

the-art for noncontact electronic skin include motion sensing by electrostatic inductions [26,27], humidity sensing by materials characteristics [28–30], *etc.* On the other hand, the need for external energy supply hampers the portability and endurance of electronic skin devices. In order to solve the energy supply problem of electronic skin sensors, energy harvester based on triboelectric nanogenerators (TENGs) [31,32] and electrets [33,34] have been widely studied. Based on such devices, the self-powered sensors [31–41] can actively generate electrical signal itself as a response to a triggering from the ambient environment without the necessity for driving power.

Herein, we present a self-powered stretchable transparent electronic skin for sensing noncontact planar linear displacements. This device is based on spatial electrostatic inductions, and it measures the motion of a matched electret which can be attached to finger. Theory is proposed to clarify the phenomenon, and simulation is conducted to compare with testing results. Patterned polydimethylsiloxane-silver nanowires (PDMS-AgNWs) thin films by spray coating are stacked to comprise the electrode-substrate double layers, while polytetrafluoroethylene (PTFE) electret is fabricated through corona charging process. The electret in this work has a long charge retention time and uniform surface charge distribution compared to energy solutions featuring TENGs. The PDMS-

* Corresponding author.

E-mail address: zhang-alice@pku.edu.cn (H. Zhang).

¹ Authors contributed equally to this work.

AgNWs thin films enhance the conductivity, transparency and stretchability of the electronic skin, while the PTFE electret acts as the signal source for motion sensing. With the voltage waveforms obtained from electrodes caused by spatial electrostatic inductions, displacement of the electret is calculated in the rectangular coordinate system with three degrees of freedom *i.e.* (x, y, α) . A digital-analog hybrid localizing method guarantees high accuracy and resolution in large area. Compare with the current noncontact electronic skins for motion sensing, our work shows a higher resolution by uniform charge distribution, better flexibility due to materials and device structure, long charge refill time, *etc.* In the meantime, such noncontact electronic skin obviates driving power by adopting a passive sensing mechanism, while providing unprecedented interacting experience as a noncontact human-machine interface.

2. Materials and methods

2.1. Fabrication of patterned PDMS-AgNWs thin film

Firstly, the PDMS base solution and the cross-linker are mixed uniformly at a mass ratio of 10:1 and evacuated for 30 min. The mixture solution is dropped on the smooth glass surface, spin-coated at 1000 rpm for 60 s and then heated on the hot plate at 80 °C for 60 min to solidify. Then a polyimide (PI) mask prepared by laser cutting is placed onto the surface of the PDMS and oxygen plasma treatment is carried out to make the surface of PDMS film hydrophilic by Corona (Electro-Technic Products, Inc. USA). After repeating spray coating ethanol solution of AgNWs, the membrane is annealed at 100 °C for 10 min to enhance conductivity and stability. Finally, the PI mask and patterned PDMS-AgNWs film are carefully peeled off sequentially.

2.2. Fabrication of noncontact electronic skin

Two PDMS-AgNWs films obtained from Section 2.1 are stacked perpendicularly while vertically connected by liquid PDMS and then heated on the hot plate at 100 °C for 10 min. At last, the device is encapsulated with liquid PDMS on the surface and then cured to protect the AgNWs exposed on the top layer. The overall thickness of the electronic skin is 600 μm .

2.3. Fabrication of PTFE electret

When the applied electric field on the corona needle exceeds the breakdown threshold of the air gap, it will cause a large amount of ions to be generated by air ionization. These ionic charges are injected into the electret under the corona electric field. Firstly, commercial polytetrafluoroethylene (PTFE, 0.5 mm in thickness) is cut into 4 cm \times 4 cm squares and then washed ultrasonically with pure water and ethanol. Next, the PTFE film is tapped onto the metal plate of the high voltage source (SPELLMAN SL1200, USA) for 10 min, with the voltage on metal grid set to be -1.6 kV , while the voltage on the corona needle is -7 kV . After measuring the surface potential distribution of the PTFE electret with electrometer (MONROE 244a), it is cut into a circle with a diameter of 2 cm using the part with uniform potential distribution.

2.4. Testing method to realize quantitative noncontact motions

In order to achieve quantitative horizontal motion with three free variables in the standard testing process, a sliding rail, a slider and an ejector are designed and 3D printed (see Fig. S1). The sliding rail is capable of translating and rotating to comply with arbitrary displacement vector (x_0, y_0, α_0) , while the PTFE electret is attached to the slider to perform motions. Electronic skin is placed directly beneath the suspended sliding rail on a coordinate paper to ensure accuracy. The vertical distance between the electret and electronic skin is fixed to 5 mm. The electric field and potential distribution generated by a

surface charge will decay over the increase of distance. Therefore, a maximum operation distance exists for this electret and the corresponding e-skin configuration to maintain a relatively high signal-noise ratio. We have tested the case when $h = 10\text{ mm}$ (see Fig. S2), and the signal-noise ratio is still very high. As a result, it is estimated that this device can work at a maximum vertical distance of three centimeters, which is convenient for regular usage as a human-machine interface. On the other hand, the vertical distance has a slight influence on the localizing functions. However, the localizing results is not very sensitive to the distance, because the localizing functions is determined by numerator over denominator, which response in the same trend to the varying distance. As a result, the normalizing effect ensures that the localizing function is insensitive to the distance, and therefore the sensing result is not very sensitive to the vertical distance. In each cycle, slider is ejected and then stopped by an interceptor to achieve designated motion with constant speed. Contrast tests are performed to verify that the sliding rail system do not produce fraud signal, since the slider is not electrified.

3. Results and discussions

The structure diagram of the electronic skin is shown in Fig. 1a, which presents the stacked electrode-substrate layers with an overlapped configuration. The five electrodes within the same layer are parallel to each other, while those within different layers are perpendicular. Ohmic contact points are reserved for connection by enlarging the AgNWs surface at the edges, and a detailed configuration of the electrodes can be found in Fig. S3a. The inset image is the photograph of a circular electret, whose noncontact motion can be characterized by the electronic skin. A picture of the electronic skin is displayed in Fig. 1b, demonstrating the excellent transparency and flexibility of the device. In addition, Fig. 1c contains the fabrication process of the electronic skin in four steps *i.e.* Oxygen plasma treatment, AgNWs spray coating, annealing and assembly. Fig. 1d is a SEM image for characterization of the AgNWs electrode. We can see from this figure that silver nanowires overlap with each other, forming the conductive network. As a tradeoff between conductivity and transparency, the AgNWs electrode has a sheet resistance of 11.9 Ω/sq , and the resistance of a 10 cm long electrode is 760 Ω in average (see Fig. S3b); whereas the overall transparency of the electronic skin is calculated as 80.2%, according to the measurement results shown in Fig. S3c. We tested the change in electrode resistance of AgNWs at different bending angles (see Fig. S4). The test results show that the resistance change of AgNWs does not exceed 100 Ω under different bending degrees. Compared with the 100 M Ω impedance of probes to the oscilloscope, the change of resistance caused by bending can be neglected. The PTFE electret fabricated by corona charging possesses an average electric potential of 2.2 kV, which is able to generate high density of stable electric field in the surrounding area which lasts for one week. Potential distribution of the electret surface can be referred in Fig. S3d. The electret has a long charge retention time for about one week. And the electret surface potential remains 80% after 7 days (see Fig. S5a). Fig. S5b also shows that the electret-based electronic skin system maintain 84% voltage output after 7 days. So that the electric field is steady and continuous over one week, despite a small decay in the magnitude of charges, which only affect the output magnitude but not the sensing results.

The working principle of the electronic skin is shown in Fig. 2. Since the electronic skin will only response to motion of the electret, it is attached to moving objects *e.g.* finger in practical usage, and taken as the token of arbitrary electrified object in simulation as well as testing. According to basic electromagnetics, surface charge imposes certain electric field distribution across the space. If equilibrium bodies and dielectrics are presented, the electric field will be altered to some extent. After setting up a two-dimensional rectangular coordinate system taking the center of the electronic skin as its origin, the electric potential of each electrode becomes the function of the position of the

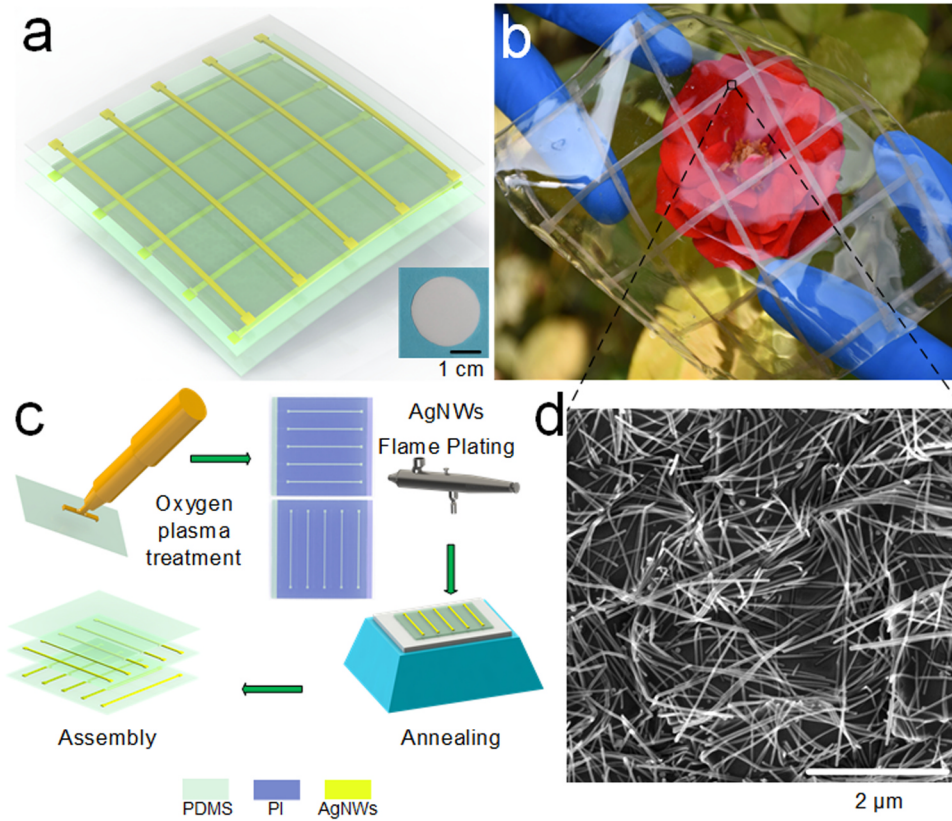


Fig. 1. Structure and fabrication process of the electronic skin. (a) The structure diagram of the electronic skin. The inset image is the photo of PTFE electric. (b) The photo of electronic skin demonstrating its transparency and stretchability. (c) The fabrication process of the noncontact electronic skin. (d) SEM image for characterization of the AgNWs network.

electret. The vertical distance between the electret and electronic skin is fixed at $h = 5$ mm for all analysis in this paper. Fig. 2d represents such function of potential in four electrodes *i.e.* E3, E2, E8 and E9 respectively. Apparently the absolute potential reaches maximum when the electret is exactly above the electrode, and the primary gradient is perpendicular to the direction of the electrode. When taking the electrostatic induction phenomenon into account, we can discover that the induced charges in the electrode is directly proportional to the potential function, because the velocity of electret is low enough for transient charges to reach equilibrium. We address the relationship between the potential and charge functions as

$$Q_i(x, y, \alpha) = \gamma U_i(x, y, \alpha) \quad (1)$$

where i corresponds to electrode number, (x, y, α) represents the coordinate of electret, and γ is the scale coefficient. Fig. 2a presents an example of displacement with a vector of $(x_0, y_0, \alpha_0) = (15 \text{ mm}, 20 \text{ mm}, 30^\circ)$. Since the matched load of the oscilloscope probe is $100 \text{ M}\Omega$ which is five orders of magnitude greater than the resistance of the AgNWs electrode, the voltage obtained by the oscilloscope can be taken as the open circuit voltage, and the induced currents can be directly calculated by dividing voltage with the load resistance. Considering the relationship between charges and currents, the voltage signals $V(t)$ measured by the oscilloscope can be therefore explicated as

$$V(t) = R_o I(t) = R_o \frac{\partial Q(t)}{\partial t} = \gamma R_o \frac{\partial U(t)}{\partial t} \quad (2)$$

$$\frac{\partial U(t)}{\partial t} = \frac{dU}{dx} \frac{dx}{dt} + \frac{dU}{dy} \frac{dy}{dt} = v(t) \left[\frac{dU}{dx} \cos \alpha + \frac{dU}{dy} \sin \alpha \right] \quad (3)$$

$$V(t) = \gamma R_o v(t) \left[\frac{dU}{dx} \cos \alpha + \frac{dU}{dy} \sin \alpha \right] \quad (4)$$

where R_o is the load resistance of the probes, v is the velocity of the electret. As a result, with electrodes perpendicular with the x axis, $\frac{dU}{dy}$ is considered noncontributing to the total value of $V(t)$, and the signal-

noise ratio is elevated when $\cos \alpha$ is significant *i.e.* α away from $\frac{\pi}{2}$. Hence, the potential response primarily to the motion component parallel to its gradient. Note that this inference is important in later analysis. Here, the acquired signal is linked with the potential distribution which can be predicted by theory. Fig. 2b displays the tested voltage waveform from four electrodes corresponding to the displacement in Fig. 2a; for the output from all ten electrodes, please refer to Fig. S6. In addition, Fig. 2d and e shows the potential distribution and curves corresponding to the displacement in the simulation results of each electrode respectively. These four electrodes are selected from the ten electrodes in total because the destination of the displacement falls into the square overlapped by these four electrodes. The similarity between the derivatives of curves in Fig. 2d and those in Fig. 2b is significant, which can serve as the evidence of the theory given above.

If a monotonous relationship between a function derived from the explicated voltage waveform $V(t)$ and the displacement vector (x_0, y_0, α_0) is discovered, we will be able to acquire the latter by calculating the former *i.e.* achieve localization by measuring signals from electrodes. Noticing the monotonicity of potential curves shown in Fig. 2e in the section inside shadowed boxes which corresponds to the shadowed square in Fig. 2a, it is promising to choose the designated area of the potential distributions and curves to construct the monotonous functions from the wave signals, in order to solve the three parameters in the displacement. As such, squares with 6.25 cm^2 become basic units, and there are 16 squares in the effective sensing area of the electronic skin in total. There is an optimal mesh size for the current device configuration in order to achieve high gradient in localizing functions and consequently the accuracy, which is related to the size of the electret and the vertical distance between the electret and electronic skin. In this work, we adopt $l = 25 \text{ mm}$ to cope with $h = 5 \text{ mm}$. With different displacement falling into these squares, we are able to pick different sets of electrodes for their signals. This method provides the basis of digital-analog hybrid electronic skin. Considering the curves shown in Fig. 2e, it can be discovered that during a single planar linear

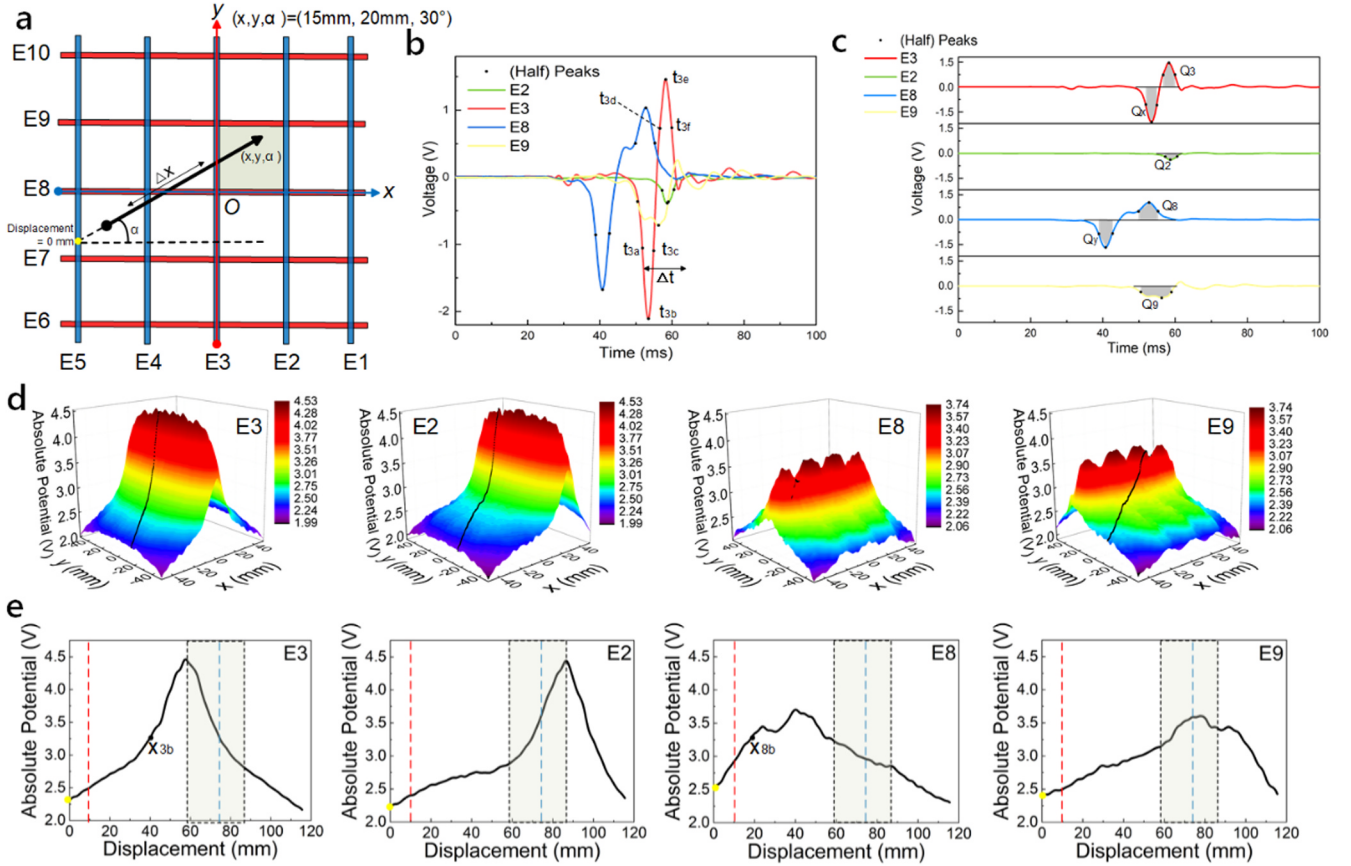


Fig. 2. Illustration of the working principle of the electronic skin. (a) An example displacement within rectangular coordinate system and the layout of electronic skin. (b) The voltage waveform obtained from testing corresponding to the displacement in (a). Peak points and half-height points are marked. (c) Same voltage waveforms in (b) with the integral along peak width at half height in the shadowed areas marked as Q . (d) function of the potentials of different electrodes with respect to the position of electret. The potential change corresponding to the displacement in (a) is shown in black dots. (e) The potential change in electrodes corresponding to the displacement of electret in (a). The shadowed box represents the area in square unit, while the red and blue dash lines marked the beginning and cease of the displacement.

motion, the monotonicity of absolute potential typically changes up to once in the designated electrodes around the square. This phenomenon is determined by the overall configuration of the electrodes. Therefore, based on electrostatic inductions, positive charges will flow into the electrodes when potential is rising, corresponding to negative peaks in Fig. 2c; while positive charges will flow away from the electrode if the absolute potential begin to decrease during the motion, corresponding to positive peaks in Fig. 2c. We find out from the above analysis that transferred charges is a monotonous function with the displacement vector (x_0, y_0, α_0) . So we will begin with constructing the localizing functions using transferred charges.

$$f(x, y, \alpha) = \frac{Q_3 + |Q_2|}{|Q_x|} \quad (5)$$

$$g(y, x, \alpha) = \frac{Q_8 + |Q_9|}{|Q_y|} \quad (6)$$

f and g are the first two localizing functions with three variables proposed. Fig. 2c demonstrates the physical meaning of Q , which is the bulk of transferred charges inside electrodes during a certain period. Q_3 and Q_8 corresponds to the positive peaks in E3 and E8 respectively; Q_2, Q_7, Q_9 corresponds to the negative peaks in E3, E2, E8, E9 respectively. Notice that transferred charges can be calculated by integrate the induced currents inside the electrodes, which are directly proportional to the voltage signal as indicated earlier. We use the integral along peak width at half height of the voltage waveforms to represent the transferred charge Q , in order to enhance the signal noise ratio by obviating the noise signal at low magnitude. Taking (1) and (2)

into account, we can explicate f and g into the following dimensionless functions

$$f(x, y, \alpha) = \frac{Q_3 + |Q_2|}{|Q_x|} = \frac{\int_{t_{3d}}^{t_{3f}} V_3(t) dt + \int_{t_{2a}}^{t_{2c}} |V_2(t)| dt}{\int_{t_{3a}}^{t_{3c}} |V_3(t)| dt} = \frac{U_3(x_{3f}, y_{3f}, \alpha_{3f}) - U_3(x_{3d}, y_{3d}, \alpha_{3d}) + U_2(x_{2a}, y_{2a}, \alpha_{2a}) - U_2(x_{2c}, y_{2c}, \alpha_{2c})}{U_3(x_{3c}, y_{3c}, \alpha_{3c}) - U_3(x_{3a}, y_{3a}, \alpha_{3a})} \quad (7)$$

$$g(y, x, \alpha) = \frac{Q_8 + |Q_9|}{|Q_y|} = \frac{\int_{t_{8d}}^{t_{8f}} V_8(t) dt + \int_{t_{9a}}^{t_{9c}} |V_9(t)| dt}{\int_{t_{8a}}^{t_{8c}} |V_8(t)| dt} = \frac{U_8(x_{8f}, y_{8f}, \alpha_{8f}) - U_8(x_{8d}, y_{8d}, \alpha_{8d}) + U_9(x_{9a}, y_{9a}, \alpha_{9a}) - U_9(x_{9c}, y_{9c}, \alpha_{9c})}{U_8(x_{8c}, y_{8c}, \alpha_{8c}) - U_8(x_{8a}, y_{8a}, \alpha_{8a})} \quad (8)$$

Taking the displacement in Fig. 2a as an example, the relevant electrodes for f will be E3 and E2, and for g they will be E8 and E9. As is indicated in Fig. 2b, t_{3b} corresponds to the negative peak point of waveform E3, while t_{3a} and t_{3c} corresponds to the left and right half-height points respectively. Similarly, t_{3d}, t_{3e} and t_{3f} stands for the positive peak from E3, and it also applies to other electrodes when changing the subscript number e.g. t_{2a} for E2, t_{8d} E8 and t_{9a} for E9. The x, y , and α related variables in the expression corresponds to the coordinate of electret at the moment t , and the subscript applies in the same way. All sets of coordinate are on the line of the displacement.

Function f and g each contains three variables i.e. x, y, α , and the essential characteristics of these functions is that they are monotonous and sensitive primarily to only one variable i.e. x and y respectively. As

is shown in Fig. 2d, gradient of potential with motion perpendicular to the electrode is much larger than that with parallel ones. As a result, the functions f and g are only sensitive to one variable, since their basic components are potentials of electrodes with respect to the position of electret. Q_x and Q_y tend to be constant values because the transferred charges when the electret is approaching the unit square tend to saturate, as long as the displacement trajectory contains $(x_{3a}, y_{3a}, \alpha_{3a})$ and $(x_{8a}, y_{8a}, \alpha_{8a})$. On the other hand, Q_3 and Q_2 increase together with x , while Q_8 and Q_9 increase together with y . This can also be illustrated by (7) and (8) if we notice the monotonicity of potential curves within the unit square. An intuitive explanation is that the electret is either approaching an electrode or departing from it within a single unit, so that the potential as well as transferred charges will change in only one direction. Because the distance between electret and four electrodes within a square unit is relatively small, the gradient of such change is significant. However, it is not enough to solve three variables with only two functions, so a third function h primarily sensitive to α is also proposed for calculations.

$$\begin{aligned}
 h(\alpha, x, y) &= \Delta x \cdot x_{ac}^{-1} = \Delta t \cdot v \cdot v^{-1} \cdot t_{ac}^{-1} = \Delta t \cdot t_{ac}^{-1} \cdot (\cos^2 \alpha + \sin^2 \alpha)^{\frac{1}{2}} \\
 &= (t_{8b} - t_{3b}) \sqrt{\left(\frac{1}{t_{3c} - t_{3a}}\right)^2 + \left(\frac{1}{t_{8c} - t_{8a}}\right)^2} \\
 &= \frac{(t_{8b} - t_{3b}) [(t_{3c} - t_{3a})^2 + (t_{8c} - t_{8a})^2]^{\frac{1}{2}}}{(t_{3c} - t_{3a})(t_{8c} - t_{8a})} \tag{9}
 \end{aligned}$$

Graphical labeling of the parameters involved can be viewed in Fig. 2a-b. x_{ac}^{-1} refers to the x and y component of displacement from t_{3a} to t_{3c} , and from t_{8a} to t_{8c} identically. Note that $t_{ac} = (t_{3c} - t_{3a})\cos\alpha = (t_{8c} - t_{8a})\sin\alpha$, and potential function $U_i(x, y, \alpha)$ is stationary, and $x_{ac}^{-1} = (x_{3c} - x_{3a})^{-1}|_{\alpha=0^\circ} = (x_{8c} - x_{8a})^{-1}|_{\alpha=90^\circ}$ is a constant value while Δx is a function of α, x and y . The physical meaning of the dimensionless function h is the displacement Δx of the electret approaching from E8 to E3 dividing a constant value x_{ac}^{-1} , and is related to all three of the variables. The meaning of dividing a constant value x_{ac}^{-1} is to make the function h irrelevant with other parameters e.g. velocity of the electret. All of the functions are irrelevant with it, as long as the velocity keeps constant through all of the t values given in the expressions. In addition, the

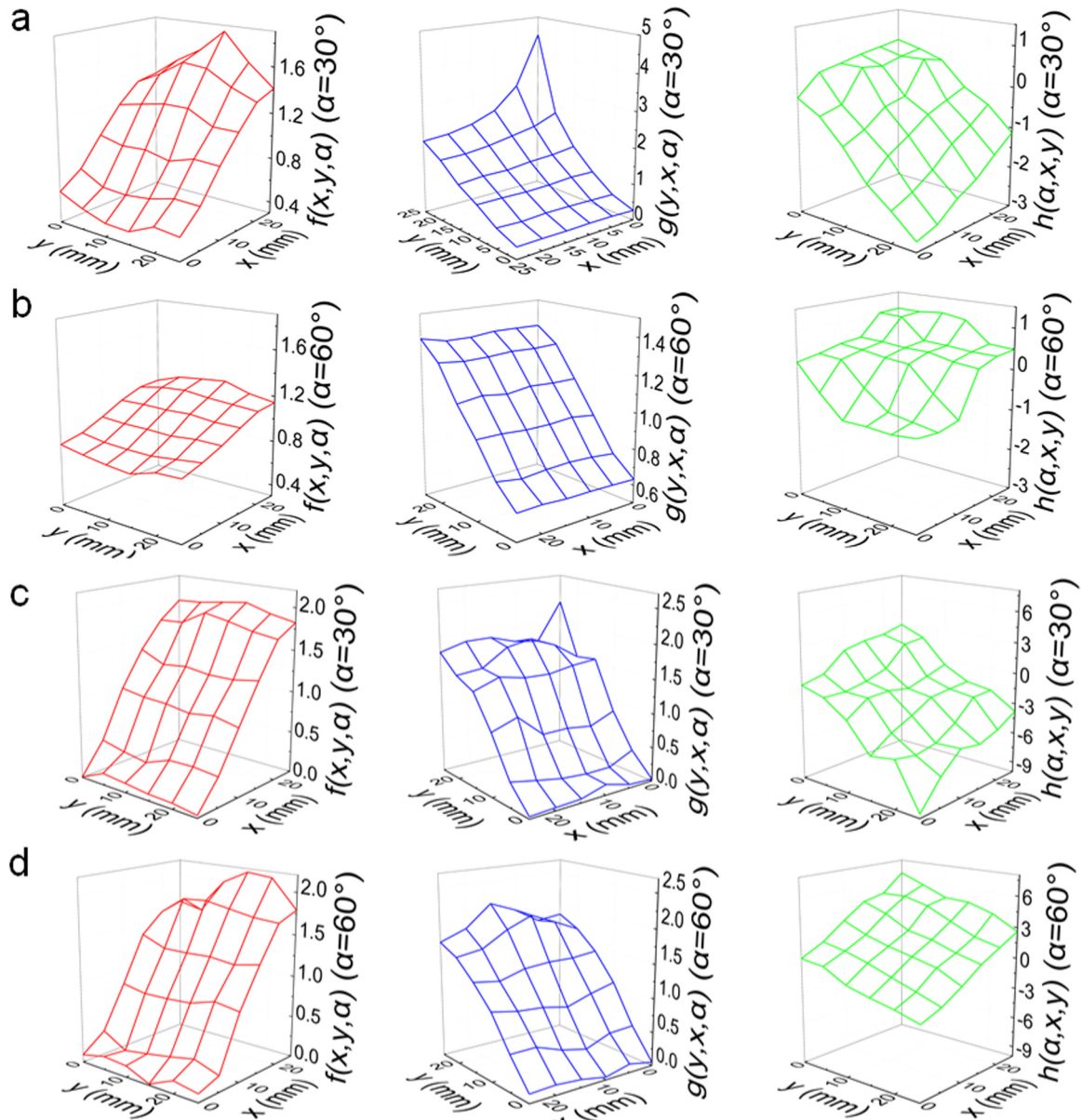


Fig. 3. Examples of localizing functions f, g , and h acquired from both simulation and testing. (a) Simulation results of f, g , and h when $\alpha = 30^\circ$. (b) Simulation results of f, g , and h when $\alpha = 60^\circ$. (c) Testing results of f, g , and h when $\alpha = 30^\circ$. (d) Testing results of f, g , and h when $\alpha = 60^\circ$.

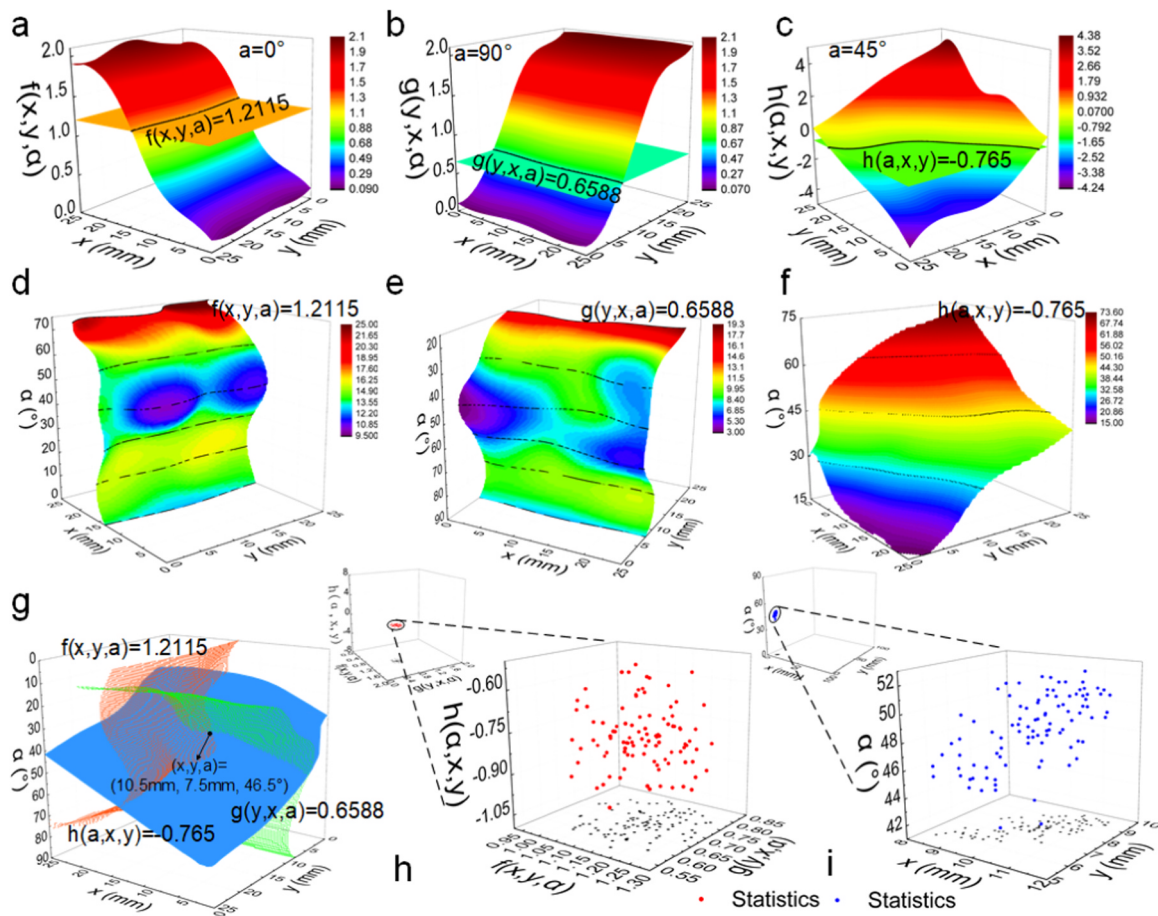


Fig. 4. Illustration of calculations for localizing results of single and repeated tests. (a) Intersection between plane $f = 1.1221$ and mesh $f(\alpha = 0^\circ)$. (b) Intersection between plane $g = 0.6588$ and mesh $g(\alpha = 90^\circ)$. (c) Intersection between plane $h = -0.765$ and mesh $h(\alpha = 45^\circ)$. (d) Contour plane $(x, y, \alpha)|_{f=1.1221}$. (e) Contour plane $(x, y, \alpha)|_{g=0.6588}$. (f) Contour plane $(x, y, \alpha)|_{h=-0.765}$. (g) Intersection between the three contour planes shown in (d), (e) and (f), with the intersecting point marked. (h) Distributions of the function values of f , g and h in the 100 repeated tests. (i) Distribution of the localization results of the 100 repeated tests.

functions are only related to the potential function of electrodes with respect to the position of electret which is fixed. Hence, these expressions apply to planar linear motion across nonadjacent unit squares with approximate constant velocity, while affected by no other variables. In f and g , the expressions only contain velocity distribution across space. While in h , the function is defined as $\Delta x \cdot x_{ac}^{-1}$, which is irrelevant with velocity. Despite that the expression is further developed to be determined by time, this function is normalized and dimensionless. Therefore, the localizing functions are irrelevant with velocity, which also apply to the sensing result. With three dimensionless functions f , g and h proposed above, we are able to achieve noncontact motion sensing by calculating values of these functions using the waveforms collected from designated electrodes in the square unit, and then compare them with standard functions to solve these coordinates.

Fig. 3a-b displays the simulation results of the three functions f , g and h for localization. In order to visualize functions with three variables, we slice them into three dimensional meshes with the third variable α fixed from 0° to 90° with an interval of 15° . We pick $\alpha = 30^\circ$ and $\alpha = 60^\circ$ as two examples, while for the complete sets of figures, please refer to Fig. S7. f ($\alpha = 90^\circ$), g ($\alpha = 0^\circ$), h ($\alpha = 90^\circ$), and h ($\alpha = 0^\circ$) is not shown in this figure because in such cases the motion is parallel to the x or y axis, and is thus unable to generate the required peaks in waveforms for possible analysis. In this figure $x, y \in [0 \text{ mm}, 25 \text{ mm}]$, which equals to the area in a square unit. In Fig. 3a-b, f (the red mesh) is monotonous with x and has good linearity, while is insensitive to y and α . In addition, g (the blue mesh) is linked with y and has good linearity, while is insensitive to x and α . In terms of h (the green mesh), this function responds monotonously with

the change of α , but is also affected by x and y . As a result, after contour planes are intercepted from the respective functions by the values obtained from testing, one and only one crossover point will be generated inevitably, and as such it is the localization result *i.e.* displacement vector (x_0, y_0, α_0) . In summary, simulation results show that these functions are capable of solving the displacement vector by processing the acquired waveforms and thus achieve noncontact localization.

Testing part provides more details about the procedure of using functions to solve the coordinates. Fig. 3c-d shows the standard testing result of three localizing functions f , g and h derived from the voltage waveforms measured from respective electrodes. I correspondence to Fig. 3a-b, we also pick $\alpha = 30^\circ$ and $\alpha = 60^\circ$ as two examples, while for the complete sets of figures, please refer to Fig. S8. The four electrodes are E3, E2, E8, E9, which is the same with Fig. 2a. The displacement vector is confined to the same unit square shown in Fig. 2a. For an arbitrary displacement falling into other square units, different sets of electrodes will be picked to measure and process these localizing functions. This paper chooses these four electrodes above for illustration. As can be seen from Fig. 3c-d, the testing results of f , g and h matches well with the simulation qualitatively. The main characteristics *i.e.* monotonicity and linearity of f , g and h with respect to x , y and α are identical between the simulation and testing results. Besides, similarity to some extent in configurations of the meshes can also be found. The range of x and y is from 0 mm to 25 mm , with an interval of 5 mm . And for α the range is $[0^\circ, 90^\circ]$, with an interval of 15° . In summary, the results of standard testing indicate accordance with theory as well as simulation, and also put the three dimensional functions in position for solving the displacement vector.

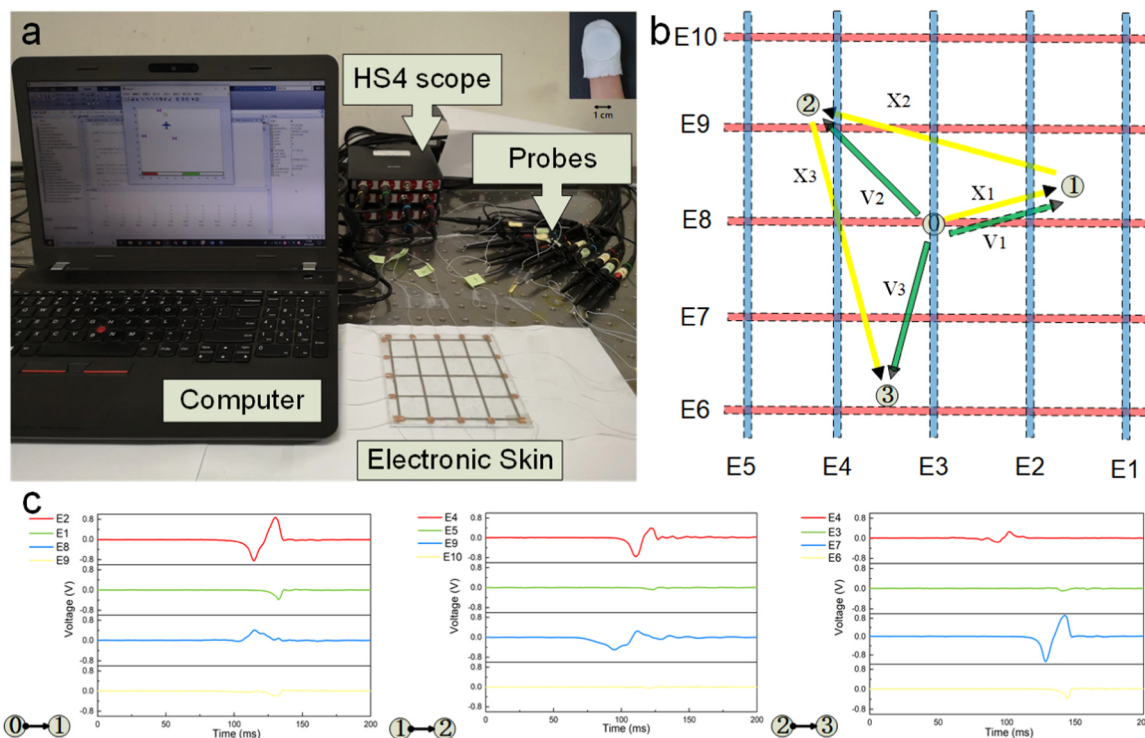


Fig. 5. Demonstration of the electronic skin as a human-machine interface. (a) The arrangement of the real-time Raiden game platform with the electronic skin serving as the human-machine interface. (b) The illustration of the sample moves of the finger in yellow arrows and the displacement of battleplane in the game in green arrows. (c) The voltage waveforms acquired by the HS4 scopes leading to the calculation of sample moves in (b).

The calculation process is illustrated in Fig. 4. A single test is performed with the displacement vector set as [10 mm, 7.5 mm, 45°]. The value of f , g and h derived from the voltage waveform is [1.1221, 0.6588, -0.765]. First the localizing functions are interpolated in three dimensions to form much denser meshes. As is shown in Fig. 4a-c, intersecting lines are made between the plane $f = 1.1221$ and the mesh $f(\alpha = 0^\circ)$, $g = 0.6588$ and the mesh $g(\alpha = 90^\circ)$, as well as $h = -0.765$ and the mesh $h(\alpha = 45^\circ)$ respectively. Assembling all intersecting lines with α from 0° to 90° , the meshes in Fig. 4d-f is formed, representing the whole contour planes $(x, y, \alpha)|_{f=1.1221}$, $(x, y, \alpha)|_{g=0.6588}$, and $(x, y, \alpha)|_{h=-0.765}$ respectively. When putting the three contour planes together in Fig. 4g, one and only one intersection point is formed, which is $(x_0, y_0, \alpha_0) = (10.5 \text{ mm}, 7.5 \text{ mm}, 48.5^\circ)$. 100 repeated tests with the same displacement vector (10 mm, 7.5 mm, 45°) are performed to investigate the accuracy and resolution of the electronic skin. The distribution of the corresponding function values is shown in 3D scatters in Fig. 4h, whereas the distribution of solved coordinates is demonstrated in Fig. 4i. The average coordinate of the 100 tests is (10.0708 mm, 7.8546 mm, 48.5025°), with an absolute deviation of (0.0708 mm, 0.3546 mm, 3.5025°) from the actual position. In addition, the standard deviation of the data is (0.7498 mm, 1.0669 mm, 2.2003°), which is excellent considering the large sensing area of 100 cm². From the outstanding results displayed above, we can conclude that this electronic skin is capable of achieving noncontact localization with high accuracy and resolution. For curved surface localization, we can extend the non-contact positioning application by recalibrating the location function (f , g , h). Here we mainly emphasize the planar displacement sensing, while the device possesses the potential for curved surface localization.

Finally, demonstration of practical usage of the self-powered non-contact electronic skin is performed, in which the device serves as a human-machine interface. Fig. 5a shows the arrangement of the real-time game platform which operates at an interval of 1 s with ~10% delay caused by signal transmission. All 10 electrodes are connected to probes from three HS4 scopes for data acquisition. The computer controls the measurement of the scopes, and extracts information from the signals acquired. As a result, users wearing a finger-cot with PTFE

electret attached on it are able to make moves in the Raiden game by sliding the index finger above the electronic skin without touching it. Fig. 5b shows three moves above the electronic skin surface marked with yellow arrows, and the corresponding displacement vectors of the battleplane in the game are marked with green arrows. The sample moves are calculated with the voltage waveforms displayed in Fig. 5c respectively; for the outputs from all ten electrodes, please refer to Fig. S9. In order to provide a more intuitive impression of such application, we prepared a supporting video (Video 1) recording the process of playing the game with electronic skin and electret as the human-machine interface. The video consists of three scenarios *i.e.* axial, diagonal and arbitrary movements, in which the user plays the game in a simple and smooth manner. Therefore, the video exhibits high accuracy of displacement sensing and excellent interacting experience of the electronic skin in the practical application.

4. Conclusions

In conclusion, we proposed a transparent stretchable electronic skin for measuring noncontact planar linear displacements. This self-powered digital-analog hybrid device is able to achieve high accuracy in large area localization with high resolution of (0.7498 mm, 1.0669 mm, 2.2003°) in all three degrees of freedom *i.e.* x , y and α . Masked AgNWs spray coating and corona charging is applied in the fabrication process of the electronic skin and the PTFE electret. Theory is proposed for explanation of the phenomenon jointing the voltage waveforms acquired from electrodes with motion of electret based on electrostatic inductions. Three dimensional functions f , g and h for calculating coordinates are developed and justified. Simulation and standard testing conducted show accordance with each other as well as the theory. When serving as a human-machine interface in a real-time game platform, this electronic skin demonstrates its feasibility in practical usage and excellence in user interacting experience. Overall, the results presented here provided fundamentals for one type of novel self-powered noncontact electronic skin; from theory to simulation, and from testing

to application. Therefore, they reveal the broad prospective of applying such kind of electronic skin into human-machine interfaces, artificial intelligence, etc.

Acknowledgement

This work was supported by National Key R&D Program of China (Grant 2018YFA0108100), National Key R&D Project from Minister of Science and Technology, China (2016YFA0202701) and the National Natural Science Foundation of China (Grant nos. 61674004, 61176103 and 91323304). The authors would also like to express their gratitude to Mr. Jianguo Jiao and Mr. Yuguang Cui for helping with fabrication of the electret.

Appendix A. Supporting information

Supplementary data associated with this article can be found in the online version at doi:10.1016/j.nanoen.2019.01.020.

References

- [1] M.L. Hammock, A. Chortos, B.C.K. Tee, J.B.H. Tok, Z. Bao, 25th anniversary article: the evolution of electronic skin (e-skin): a brief history, design considerations, and recent progress, *Adv. Mater.* 25 (2013) 5997–6038.
- [2] X. Wang, et al., Recent progress in electronic skin, *Adv. Sci.* 2 (2015) 1500169.
- [3] Y. Fu, et al., A self-powered brain multi-perception receptor for sensory-substitution application, *Nano Energy* 44 (2018) 43–52.
- [4] W. Gao, et al., Fully integrated wearable sensor arrays for multiplexed in situ perspiration analysis, *Nature* 529 (2016) 509.
- [5] J.J. Norton, et al., Soft, curved electrode systems capable of integration on the auricle as a persistent brain-computer interface, *Proc. Natl. Acad. Sci.* (2015) 201424875.
- [6] X. Xue, Y. Fu, Q. Wang, L. Xing, Y. Zhang, Outputting olfactory bionic electric impulse by PANI/PTFE/PANI sandwich nanostructures and their application as flexible, smelling electronic skin, *Adv. Funct. Mater.* 26 (2016) 3128–3138.
- [7] D.H. Ho, et al., Stretchable and multimodal all graphene electronic skin, *Adv. Mater.* 28 (2016) 2601–2608.
- [8] G.Y. Bae, et al., Pressure/Temperature Sensing Bimodal Electronic Skin with Stimulus Discriminability and Linear Sensitivity, *Adv. Mater.* (2018) 1803388.
- [9] S. Zhao, R. Zhu, Electronic skin with multifunction sensors based on thermo-sensation, *Adv. Mater.* 29 (2017) 1606151.
- [10] S. Han, et al., Mechanically reinforced skin-electronics with networked nanocomposite elastomer, *Adv. Mater.* 28 (2016) 10257–10265.
- [11] Y. Dai, et al., A self-powered brain-linked vision electronic-skin based on triboelectric-Photodetecting pixel-addressable matrix for visual-image recognition and behavior intervention, *Adv. Funct. Mater.* 28 (2018) 1800275.
- [12] W. Wu, X. Wen, Z.L. Wang, Taxel-addressable matrix of vertical-nanowire piezotronic transistors for active/adaptive tactile imaging, *Science* (2013) 1234855.
- [13] J. Kang, et al., Tough and water-insensitive self-healing elastomer for robust electronic skin, *Adv. Mater.* 30 (2018) 1706846.
- [14] Y.C. Lai, et al., Extraordinarily sensitive and low-voltage operational cloth-based electronic skin for wearable sensing and multifunctional integration uses: a tactile-induced insulating-to-conducting transition, *Adv. Funct. Mater.* 26 (2016) 1286–1295.
- [15] K. Hu, et al., Self-powered electronic skin with biotactile selectivity, *Adv. Mater.* 28 (2016) 3549–3556.
- [16] S. Wang, et al., Skin electronics from scalable fabrication of an intrinsically stretchable transistor array, *Nature* 555 (2018) 83.
- [17] D. Son, et al., An integrated self-healable electronic skin system fabricated via dynamic reconstruction of a nanostructured conducting network, *Nat. Nanotechnol.* (2018) 1.
- [18] Q. Sun, et al., Active matrix electronic skin strain sensor based on piezo-potential-powered graphene transistors, *Adv. Mater.* 27 (2015) 3411–3417.
- [19] S.H. Kim, et al., Ultrastretchable conductor fabricated on skin-like hydrogel-elastomer hybrid substrates for skin electronics, *Adv. Mater.* (2018) 1800109.
- [20] D. Kang, et al., Ultrasensitive mechanical crack-based sensor inspired by the spider sensory system, *Nature* 516 (2014) 222.
- [21] C. Pang, et al., A flexible and highly sensitive strain-gauge sensor using reversible interlocking of nanofibres, *Nat. Mater.* 11 (2012) 795.
- [22] K. Dong, et al., A Stretchable yarn embedded triboelectric nanogenerator as electronic skin for biomechanical energy harvesting and multifunctional pressure sensing, *Adv. Mater.* (2018) 1804944.
- [23] M. Park, et al., MoS₂-based tactile sensor for electronic skin applications, *Adv. Mater.* 28 (2016) 2556–2562.
- [24] Y. Qiao, Multilayer graphene epidermal electronic skin, *ACS Nano* (2018).
- [25] H. Wu, et al., Self-powered noncontact electronic skin for motion sensing, *Adv. Funct. Mater.* 28 (2018) 1704641.
- [26] M. Shi, et al., Self-powered analogue smart skin, *ACS nano* 10 (2016) 4083–4091.
- [27] M.U. Mutlu, O. Akin, M.M. Demir, Ü.H. Yildiz, *Materials Science Forum*, 915 Trans

- Tech Publ, 2018, pp. 207–212.
- [28] J. An, et al., All-graphene-based highly flexible noncontact electronic skin, *ACS Appl. Mater. Interfaces* 9 (2017) 44593–44601.
- [29] X. Wang, Z. Xiong, Z. Liu, T. Zhang, Exfoliation at the liquid/air interface to assemble reduced graphene oxide ultrathin films for a flexible noncontact sensing device, *Adv. Mater.* 27 (2015) 1370–1375.
- [30] Y.-L. Tai, Z.-G. Yang, Flexible, transparent, thickness-controllable SWCNT/PEDOT: PSS hybrid films based on coffee-ring lithography for functional noncontact sensing device, *Langmuir* 31 (2015) 13257–13264.
- [31] F.-R. Fan, Z.-Q. Tian, Z.L. Wang, Flexible triboelectric generator, *Nano Energy* 1 (2012) 328–334.
- [32] S. Niu, Z.L. Wang, Theoretical systems of triboelectric nanogenerators, *Nano Energy* 14 (2015) 161–192.
- [33] Y. Wu, Y. Hu, Z. Huang, C. Lee, F. Wang, Electret-material enhanced triboelectric energy harvesting from air flow for self-powered wireless temperature sensor network, *Sens. Actuators A: Phys.* 271 (2018) 364–372.
- [34] B. Wang, et al., Sandwiched composite fluorocarbon film for flexible electret generator, *Adv. Electron. Mater.* 2 (2016) 1500408.
- [35] S. Wang, L. Lin, Z.L. Wang, Triboelectric nanogenerators as self-powered active sensors, *Nano Energy* 11 (2015) 436–462.
- [36] X. Chen, et al., Flexible fiber-based hybrid nanogenerator for biomechanical energy harvesting and physiological monitoring, *Nano Energy* 38 (2017) 43–50.
- [37] M. Shi, et al., Self-powered wireless smart patch for healthcare monitoring, *Nano Energy* 32 (2017) 479–487.
- [38] H. Chen, et al., Fingertip-inspired electronic skin based on triboelectric sliding sensing and porous piezoresistive pressure detection, *Nano Energy* 40 (2017) 65–72.
- [39] Y. Song, et al., Highly compressible integrated super-capacitor-piezoresistance-sensor system with CNT-PDMS sponge for health monitoring, *small* 13 (2017) 1702091.
- [40] X. Cheng, et al., High efficiency power management and charge boosting strategy for a triboelectric nanogenerator, *Nano Energy* 38 (2017) 438–446.
- [41] J. Zhu, et al., A flexible comb electrode triboelectric-electret nanogenerator with separated microfibers for a self-powered position, motion direction and acceleration tracking sensor, *J. Mater. Chem. A* 6 (2018) 16548–16555.



Hang Guo received his B.S. degree from Huazhong University of Science and Technology (HUST) in 2017 and now is a Ph.D. student at Academy for Advanced Interdisciplinary Studies in Peking University. His research interests focus on electronic skin and self-powered nano-systems.



Hanxiang Wu received his B.S. degree in Microelectronics from Peking University, China, in 2018. He is currently pursuing the Ph.D. degree at the Department of Materials Science and Engineering, University of California, Los Angeles, USA. His current research interest is flexible electronics.



Yu Song received the B.S. degree in Electronic Science & Technology from Huazhong University of Science and Technology, China, in 2015. He is currently pursuing the Ph.D. degree at the National Key Laboratory of Nano/Micro Fabrication Technology, Peking University, Beijing, China. He majors in MEMS and his research is focusing on supercapacitors and self-charging power system.



Liming Miao received the B.S. degree from Peking University, Beijing, in 2017. His research interests mainly include wrinkle structure and triboelectric nanogenerator.



Zongming Su received the B.S. degree from the University of Science and Technology Beijing, in 2013. He received the Ph.D. degree in microelectronics from Peking University, Beijing, in 2018. His research interests are micro & Nano structure fabrication and energy harvesting.



Xuexian Chen received the B.S. degree from the University of Electronic Science and Technology of China, Chengdu, in 2015. She is currently pursuing the Ph.D. degree at the National Key Laboratory of Nano/Micro Fabrication Technology, Peking University, Beijing, China. Her research interests mainly include design and fabrication of hybrid nanogenerator and electrospinning process.



Mengdi Han received the B.S. degree in Electronic Science & Technology from the Huazhong University of Science and Technology, China, in 2012. He received the Ph.D. degree in microelectronics from Peking University, Beijing, in 2017. His research work is focused on flexible electronics and energy harvesting.



Haotian Chen received the B. S. degree from Dalian University of Technology, China, in 2013. He received the Ph.D. degree in microelectronics from Peking University, Beijing, in 2018. His research mainly focuses on energy harvesters and electronic skins.



Hai-Xia (Alice) Zhang received the Ph.D. degree in mechanical engineering from Huazhong University of Science and Technology, Wuhan, China, 1998. She is currently a Professor with the Institute of Microelectronics, Peking University, Beijing, China. She joined the faculty of the Institute of Microelectronics in 2001 after finishing her post-doctoral research in Tsinghua University. Her research interests include MEMS design and fabrication technology, SiC MEMS, and micro energy technology.